*Materials Research*. 2025; 28: e20250452
DOI: https://doi.org/10.1590/1980-5373-MR-2025-0452

# Effects of Surface Preparation on the Corrosion Resistance of TSA Anodized Aluminum Alloys

***Bruno Nogueira Pereira*[a], *João Victor de Sousa Araujo*[a*], *Rafael Emil Klumpp*[a],**

***Renato Altobelli Antunes*[b], *Isolda Costa*[a]**

[a]*Instituto de Pesquisas Energéticas e Nucleares, São Paulo, SP, Brasil.*
[b]*Universidade Federal do ABC, Centro de Engenharia, Modelagem e Ciências Sociais Aplicadas, Santo André, SP, Brasil.*

Received: May 13, 2025; Revised: October 13, 2025; Accepted: October 26, 2025

This study examines the impact of surface preparation on the corrosion resistance of anodized AA2198-T851 aluminum alloy. Two pretreatment methods were employed: (i) alkaline degreasing in 10 wt.% NaOH at 60 °C followed by de-smutting in 30 vol.% $HNO_3$, and (ii) etching in an oxidizing acidic solution ($K_3$ Smutt-Go, 7 V, 20 °C) intended to remove copper-containing intermetallic particles. Surface preparation methods were analyzed using SEM, FEG-SEM, SEM-EDS, and XPS. Corrosion resistance was tested through EIS, and NSST. All electrochemical tests were conducted in 0.1 mol $L^{-1}$ NaCl solution, and the NSST followed ASTM B117-16. The findings show that removing intermetallic particles greatly improves the corrosion resistance of TSA-anodized AA2198-T851. Among the tested conditions, the etched samples exhibited superior performance, showing no observable corrosion after 336 hours of salt spray exposure, confirming their enhanced corrosion resistance.

**Keywords:** *AA2198-T851 Al-Cu-Li alloy, Anodizing, Corrosion protection, Surface pretreatment.*

## 1. Introduction

Aluminum alloys are important in the production of structural materials, especially in the aerospace sector. With high mechanical strength, low density, and good machinability and workability, they are suitable for both commercial and military aerospace uses, where reducing weight affects fuel efficiency[1-7]. Aluminum alloys are increasingly used in the automotive sector to reduce $CO_2$ emissions and as lightweight materials, especially in electric vehicles.

The new Al-Cu-Li alloys, specifically AA2198, provide structural advantages for aircraft, including weight reduction and enhanced fatigue crack growth resistance[8-10]. The incorporation of Li (1 wt.% Li decreases the density of alloy by approximately 3%) makes AA2198 a potential substitute for AA2024[11-13]. However, Al-Cu-Li alloys are highly susceptible to localized corrosion, primarily due to microstructural heterogeneities, including T1 ($Al_2CuLi$), δ′ ($Al_3Li$), Θ'/Θ" ($Al_2Cu$), and S ($Al_2CuMg$) phases. While these precipitates contribute to alloy strengthening, they also increase susceptibility to localized corrosion due to micro-galvanic effects[12-17].

To enhance the corrosion resistance of aluminum alloys, surface treatments are commonly employed[1,2,14,18-20]. Among them, anodizing is widely used, as the anodic oxide layer not only improves corrosion protection but also enhances adhesion for primers and paints[21-25].

Several studies have explored the relationship between intermetallic particles and the quality of the anodic film in Al-Cu-Li alloys[26,27]. Ma et al.[28] reported a correlation between localized corrosion in TSA-anodized AA2099-T8 and the presence of Cu-enriched intermetallic particles. Similarly, Wu et al.[29] found that coarse intermetallic particles can cause defects in the anodic film, as they partially dissolve during TSA anodizing, leaving behind copper-rich residual particles that promote localized corrosion. Indeed, previous research has reported poor corrosion resistance of TSA-anodized Al-Cu-Li alloys in salt spray tests[14,29-34].

Moreover, recent studies[35-38] have investigated the behavior of micrometric particles in the AA2198-T8 alloy during anodizing at different voltages, demonstrating that the preferential dissolution of these particles can lead to defects in the anodic film and cavities on the anodized surface. These findings highlight the importance of anodizing parameters in determining the quality of the protective coating and the corrosion resistance of the alloy. However, despite these insights, there is still a gap in the literature regarding the effect of surface preparation on the corrosion resistance of anodized AA2198 alloys.

Thus, this study aims to investigate the influence of surface preparation on the corrosion resistance of TSA-anodized AA2198-T851 alloy, providing new insights into the optimization of pretreatment processes for improved corrosion performance.

## 2. Experimental

### *2.1. Materials and surface preparation*

AA2198-T851 aluminum alloy was used in this study, with the following chemical composition (wt.%): Cu 3.31, Li 0.96, Mg 0.31, Si 0.03, Fe 0.04, Ag 0.25, Zr 0.4, Zn 0.01, and Al (balance).

*e-mail: jvaraujo@alumni.usp.br
**Associate Editor:** José Daniel Biasoli de Mello.
**Editor-in-Chief:** Luiz Antonio Pessan.

The alloy surface was prepared for anodizing using two distinct pretreatment methods:

- Alkaline Degreasing: The samples were immersed in a 10 wt.% NaOH solution at 60°C for 60 s, followed by de-smutting in a 30 vol.% $HNO_3$ solution at room temperature for 30 s.
- Etching: The samples were first degreased in ethanol, then immersed in an oxidizing/acidic solution (K3 Smutt-Go) at 20 °C for 10 min under the application of 7 V, aiming to remove coarse intermetallic (IM) particles.

After pretreatment, the samples were anodized in tartaric-sulfuric acid (TSA) solution, containing 40 g $L^{-1}$ of sulfuric acid and 80 g $L^{-1}$ of tartaric acid. The anodizing process was carried out using a Biologic SP-300 potentiostat, with the aluminium sample (anodic area of 16 $cm^2$) as the working electrode and a titanium electrode coated with platinum (area of 40 $cm^2$) as the counter electrode, positioned at a distance of 10 cm. The electrolyte volume was 1 L and was continuously agitated during anodizing. The temperature was maintained at 37 °C, and a constant potential of 14 V was applied for 20 min. For samples exposed to the Neutral Salt Spray Test (NSST), the anodized layers were sealed in deionized water at 100 °C for 20 min. The NSST was performed in accordance with ASTM B117-16 for 336 hours.

### *2.2. Sample preparation for analysis*

Samples were mechanically ground using SiC papers, followed by polishing with 1 µm diamond suspension. Before analysis, samples were degreased in ethanol, rinsed with deionized water, and stored in a desiccator to prevent contamination.

### *2.3. Electrochemical impedance spectroscopy (EIS)*

EIS measurements were conducted in a 0.1 M NaCl solution using a Bio-Logic SP-200 potentiostat. A three-electrode system was employed, consisting of:

- Working electrode: AA2198 sample (1 $cm^2$ exposed surface)
- Counter electrode: Platinum (Pt)
- Reference electrode: Ag/AgCl (saturated KCl)

Prior to each EIS test, the specimens were immersed in the electrolyte for 10 h to reach a stable open-circuit potential (OCP). The measurements were performed by applying a sinusoidal perturbation of 10 mV around the OCP. EIS spectra were recorded over a frequency range of 50 kHz to 10 mHz, with 10 points per decade. The data were processed using EC-Lab® software (Bio-Logic).

### *2.4. Surface morphology and elemental analysis*

Scanning Electron Microscopy (SEM) was conducted using a Hitachi TM 3000 microscope equipped with an Energy-Dispersive X-ray Spectroscopy (EDS) detector. An acceleration voltage of 15 kV was employed for SEM-EDS analyses. Field Emission Gun - Scanning Electron Microscopy (FEG-SEM) was performed using a JEOL JSM 6010 microscope, also equipped with a Thermo UltraDry™ EDS detector. The acceleration voltage used for FEG-SEM observations was 5 kV.

### *2.5. X-ray photoelectron spectroscopy (XPS)*

XPS analysis was conducted using a ThermoFisher Scientific K-Alpha+ spectrometer with a monochromated Al-Kα radiation source (1486.6 eV) and a 400 µm spot size to maximize signal collection. High-resolution spectra were recorded using a pass energy of 50 eV. Peak fitting was carried out using a Gaussian-Lorentzian function within the Avantage™ software, employing the Smart background subtraction algorithm. The binding energy scale was calibrated by referencing C1s at 284.8 eV.

## 3. Results

### *3.1. Surface morphology before and after pretreatment*

Figure 1 presents Scanning Electron Microscopy (SEM) images of the AA2198-T851 sample in the polished

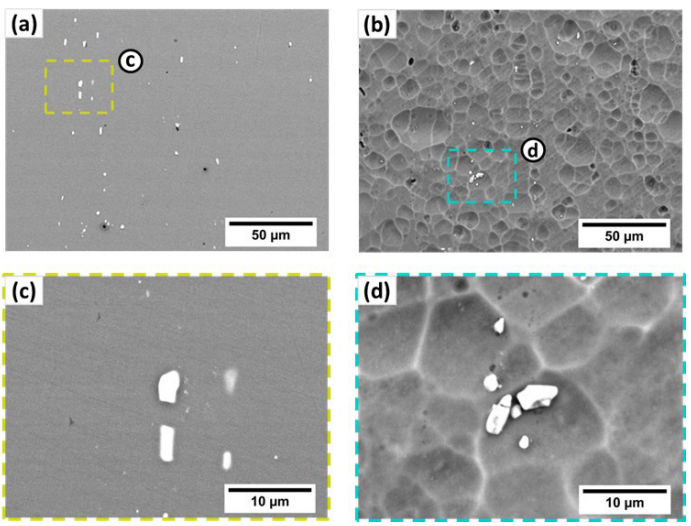


**Figure 1.** SEM images of AA 2198-T851: (a- c), polished surface showing bright intermetallic particles, (b-d) after alkaline degreasing, with intermetallics and small cavities on the aluminum matrix.

condition and after alkaline degreasing. Images (a) and (c) correspond to the polished sample: in (a), a general view at low magnification reveals intermetallic particles with bright contrast, indicating a higher density compared to the matrix; in (c), a higher magnification highlights a region containing these intermetallics. Images (b) and (d) refer to the sample after alkaline degreasing: (b) shows the general view, while (d) presents a magnified area where intermetallic particles remain visible, still exhibiting bright contrast.

Polishing clearly enhanced the visibility of the intermetallics, and after alkaline degreasing, the aluminum surface shows small cavities resulting from matrix attack, without complete removal of the intermetallic particles.

Figure 2 presents SEM images of the AA2198-T851 alloy before (a–c) and after (d–f) coarse intermetallic particle (IM) removal etching pretreatment.

Prior to etching, the alloy surface contains coarse intermetallic (IM) particles, predominantly Fe- and Cu-rich phases. This observation is further confirmed by the SEM-EDS elemental maps in Figure 3, where image (a) represents the alloy before etching and image (e) after etching.

Etching pretreatment resulted in the detachment of IM particles, leaving behind cavities on the surface. As seen in Figure 2 (d–f) and Figure 3 (e), nearly all IM particles were removed, including those within surface cavities. Donatus et al.[12] previously characterized these particles in AA2198-T851, identifying them as Fe- and Cu-rich IM phases with varying Fe:Cu ratios.

### *3.2. Anodic film morphology*

Figure 4 presents FEG-SEM images of TSA-anodized AA2198-T851 after alkaline degreasing and etching, revealing the porous characteristic of the anodic film morphology with central pores of approximately 10 nm in diameter[21,39,40].

The etched sample Figure 4 (b) exhibits a higher concentration of pores in the anodic layer compared to the alkaline-degreased sample. ImageJ analysis quantifies the pore area percentage for each pretreatment, showing 5.9% for etching and 10.1% for alkaline degreasing, indicating a more compact oxide structure in the former. However, the mean pore diameter remains similar between treatments, with values of (11.1 ± 0.2) nm for alkaline degreasing and

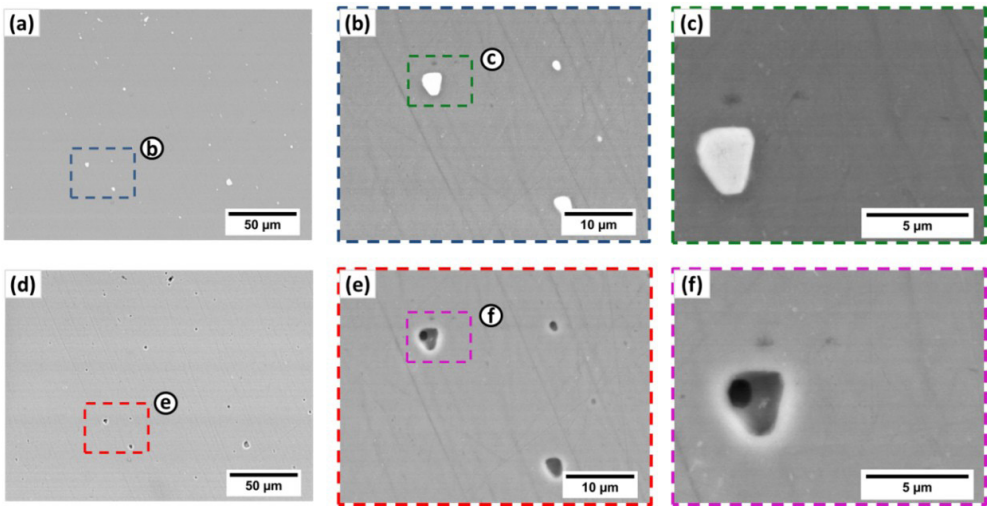


**Figure 2.** SEM images of AA 2198-T851: (a), (b), and (c) before etching pretreatment; (d), (e), and (f) after etching pretreatment.

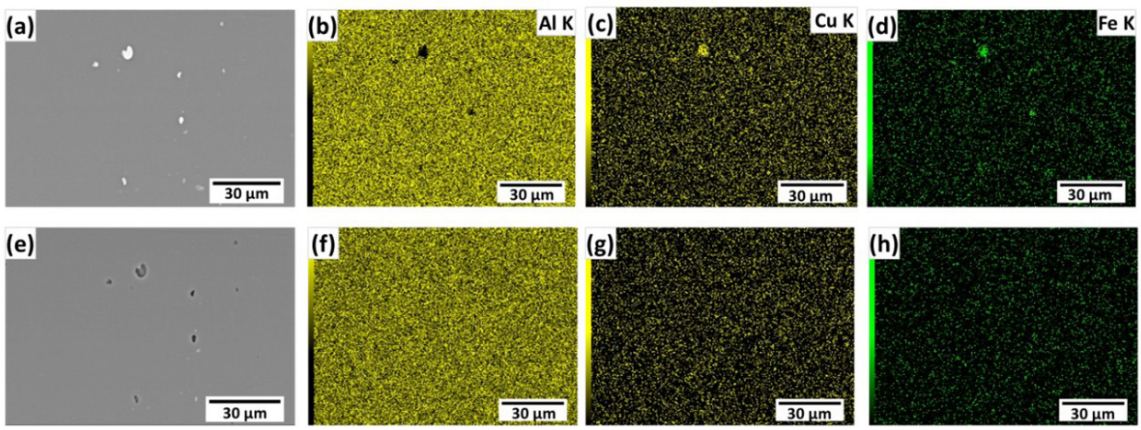


**Figure 3.** EDS maps of the surface of AA2198-T851: (a), (b), (c), and (d) before etching pretreatment; (e), (f), (g), and (h) after etching pretreatment.

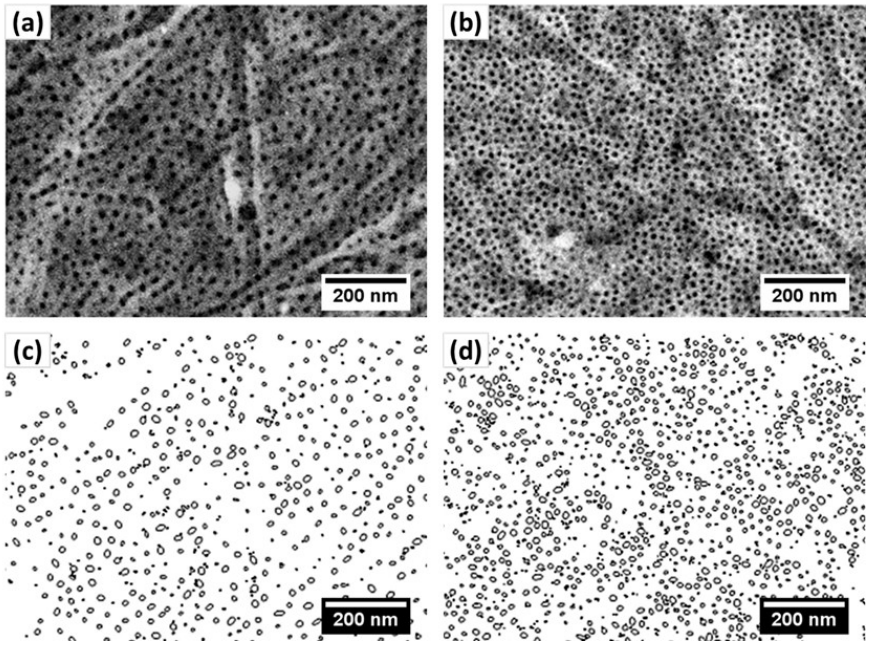


**Figure 4.** FEG-SEM images of TSA-anodized AA 2198-T851: (a) and (c) after alkaline degreasing; (b) and (d) after etching pretreatment.

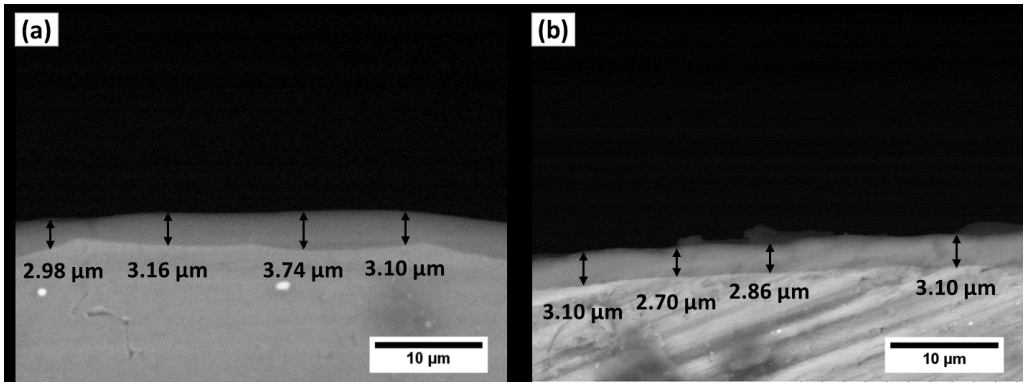


**Figure 5.** SEM cross-sectional images of TSA-anodized AA 2198-T851: (a) after alkaline degreasing; (b) after etching pretreatment.

(11.0 ± 0.1) nm for etching. This consistency in pore diameter agrees with the Field-Assisted Dissolution (FAD) model[21,23], which predicts that both the barrier-layer thickness and pore diameter scale linearly with the anodizing voltage. Since the anodizing voltage was identical for both conditions (14 V), the resulting pore diameters are expected to be comparable. Nevertheless, the different surface conditions prior to anodizing affect pore nucleation and distribution, leading to the observed variation in pore density.

Figure 5 presents SEM cross-sectional images of TSA-anodized AA2198-T851, showing anodic layer thicknesses of (3.25 ± 0.54) µm for the alkaline-degreased sample and (3.25 ± 0.27) µm for the etched sample.

These values align with literature reports for TSA-anodized aluminum alloys[21,22,41,42], reinforcing the consistency of the anodizing process.

Figure 6 presents the current density-time response for AA2198-T851 anodizing after alkaline degreasing (red curve)

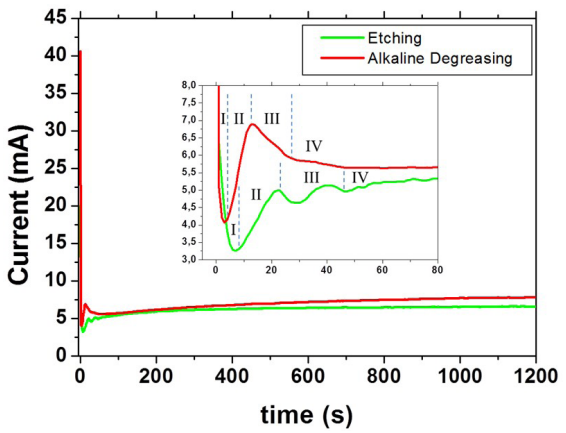


**Figure 6.** Anodizing behavior of AA 2198-T851 alloy in TSA electrolyte under potentiostatic conditions (14 V, 37°C): current density vs. time response.

and etching (green curve). Initially, both curves exhibit a sharp current peak, attributed to the breakdown of the thin naturally formed oxide layer under high applied potential[43].

The rapid current drop that follows corresponds to barrier layer formation (Stage I), where oxide growth reduces electron transport. The gradual increase in current (Stage II) is associated with pore nucleation, consistent with the Field-Assisted Dissolution (FAD) model[21,23,40,43,44]. The etched sample displays a more gradual current increase compared to the alkaline-degreased sample, suggesting differences in pore nucleation dynamics and aligning with the higher porosity observed in FEG-SEM images (Figure 4). The final stages correspond to pore formation (Stage III) and porous film growth (Stage IV). These findings suggest that etching pretreatment alters the oxide formation process, leading to distinct barrier layer and porous layer characteristics.

### *3.4 Electrochemical impedance spectroscopy (EIS) analysis*

Figure 7 shows the EIS measurements for unsealed TSA-anodized AA2198-T851 in 0.1 M NaCl solution after 2 h of immersion, comparing alkaline-degreased (red) and etched (green) samples.

Phase angle plots of Figure 7 (a) reveal two-time constants, corresponding to the barrier layer (low-frequency, LF) and the porous anodic layer (high-frequency, HF)[22,39,40,45]. The etched sample exhibits a broader phase angle, indicating a more compact and protective barrier layer.

To model the anodic coating, a two-time-constant equivalent circuit was used, Figure 7 (b), considering the partial pore sealing effect caused by the dissolution of anhydrous alumina and precipitation of hydrated alumina[22,45]. Due to the non-homogeneous nature of the anodic layer, Constant Phase Elements (CPEs) were used instead of ideal capacitors. The fitted parameters are shown in Table 1.

The sample exposed to etching presented lesser capacitive behavior than that after alkaline degreasing as indicated by the time constant at high frequency (HF) to medium frequency (MF). The fitted results display a similar value of porous layer resistance (Rp) for both samples. This resistance includes the effects of electrolyte in the pores and its corresponding value of CPEp corresponds to capacitance of the porous layer.

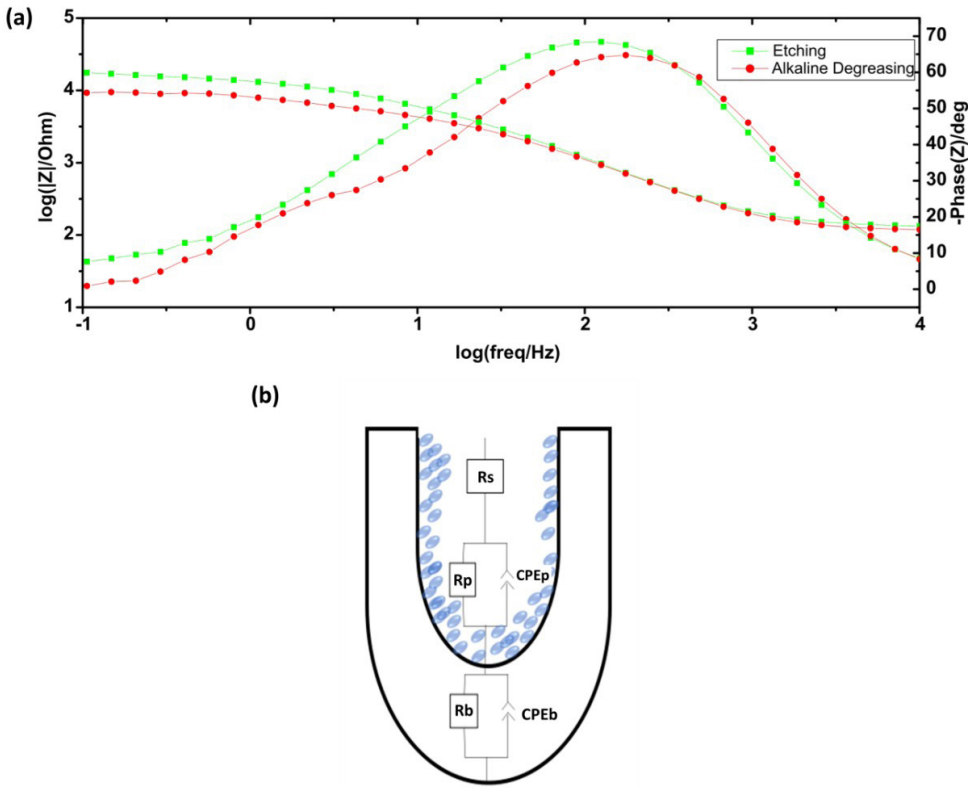


**Figure 7.** EIS plots of TSA-anodized AA 2198-T851 samples after 2 h of exposure in 0.1 mol $L^{-1}$ NaCl solution: (a) Bode diagram and (b) schematic representation of the pore and circuit elements.

**Table 1.** Electrochemical impedance spectroscopy (EIS) fitting parameters for unsealed TSA-anodized AA2198-T851 after different surface pretreatments.

| Sample | CPEp ($F.s^{(n-1)}$) | n | Rp $Ohm.cm^2$ | CPEb ($F.s^{(n-1)}$) | n | Rb $Ohm.cm^2$ |
|---|---|---|---|---|---|---|
| **Etching** | $0.199x10^{-5}$ | 0.98 | 4393 | $3.917x10^{-5}$ | 0.85 | 14221 |
| **Alkaline Degreasing** | $3.147x10^{-5}$ | 0.90 | 3871 | $2.154x10^{-4}$ | 0.87 | 5634 |

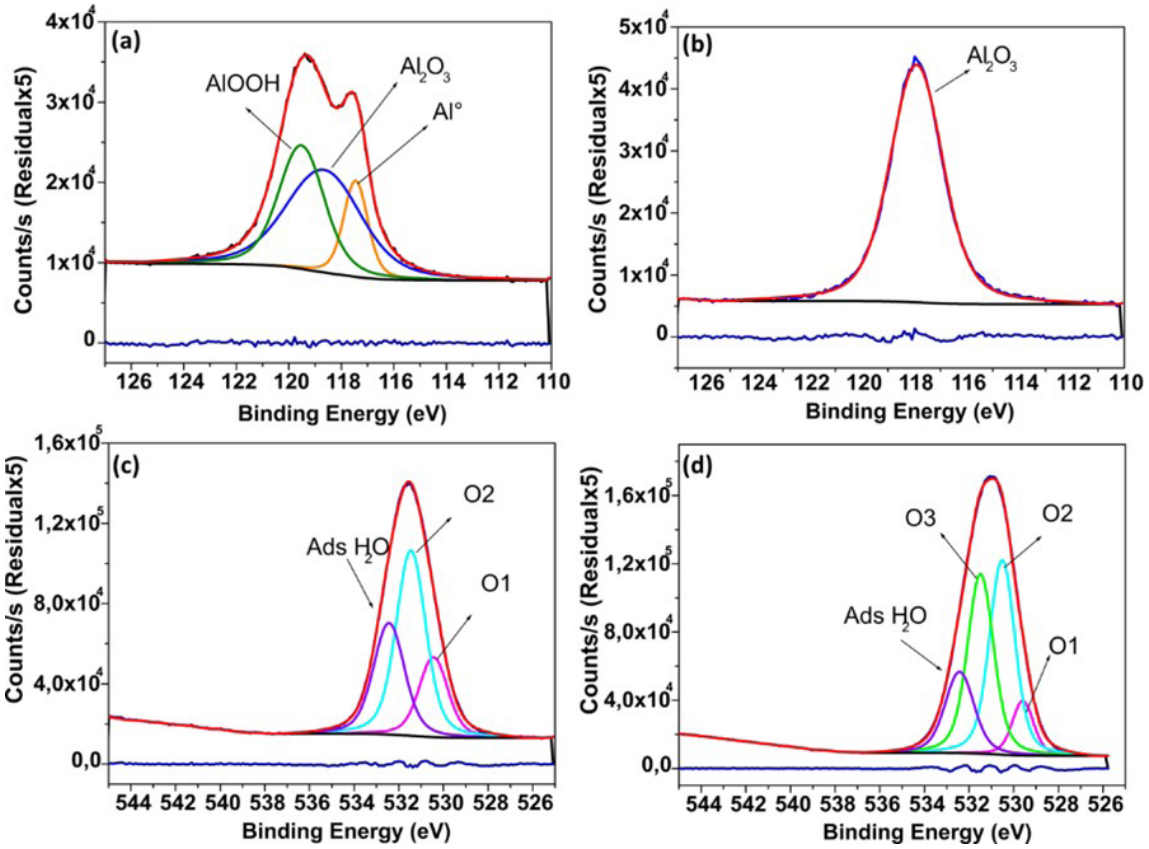


**Figure 8.** XPS high-resolution spectra of AA2198-T851: (a) Al 2p region of the alkaline-degreased surface; (b) Al 2p region of the etched surface; (c) Al 2p region of the alkaline-degreased; (d) O 1s region of the etched surface.

A discrepancy is noticed for the LF frequency range, related to the barrier layer, which is mainly responsible for the resistance to corrosion, which is described by a resistance Rb and a capacitance CPEb[22,40,42,45]. The samples after etching showed higher LF impedance modulus than that after alkaline degreasing, indicating higher corrosion resistance. The fitted results displayed a resistance (Rb) approximately three times higher. These results suggest that the main difference produced in the pretreatment is in the barrier layer and indicate that the barrier layer formed in the etched sample presents less conductive pathways for aggressive electrolyte penetration.

### *3.5 X-ray photoelectron spectroscopy (XPS) analysis*

The XPS data as high-resolution spectra of AA2198-T851 corresponding to the alkaline degreased and etched surfaces are presented in Figure 8.

The high-resolution spectra for Al2p region corresponding to the degreased surface are shown in Figure 8 (a). The Al2p was deconvoluted into three components. There is a well-defined Al° peak at low energy[46,47]. The other two components were respectively attributed to $Al_2O_3$ and AlOOH[48,49]. Differently, the Al2p high-resolution spectra related to the etched sample Figure 8 (b) was deconvoluted with only one component (attributed to $Al_2O_3$ film). This result suggests an alteration on the surface sample due the pretreatment that provided a more homogenous surface. Surface composition modification is also noted in the high-resolution spectra for O1s. The O1s for alkaline degreased sample was deconvoluted in three components (O1, O2, and Ads water) where O1 (530.45 eV) is attributed to $O^{2-}$, O2 (531.45) to $OH^-$, and the peak at 532.44 eV to adsorbed water on the alumina film[48-51]. The O1 peak corresponding to the etched sample was deconvoluted in four components (O1, O2, O3, and Ads Water). The literature suggests that the additional peak (O1 at 529.29 eV) is due to hydrated alumina $Al(OH)_3$[48]. It is important to notice that the etching pretreatment changes the composition of the surface.

### *3.6 Corrosion performance in salt spray test (NSST)*

Figure 9 presents the visual evolution of unsealed TSA-anodized AA2198-T851 during neutral salt spray testing (NSST), comparing alkaline-degreased and etched samples over 48 h, and 336 h of exposure.

The alkaline-degreased sample exhibited pitting corrosion before 48 h, with extensive corrosion sites observed after 336 h. In contrast, the etched sample showed no visible corrosion after 336 h, showing greater corrosion resistance. These observations correlate well with EIS results, further supporting the enhanced barrier properties of the anodic film formed on the etched surfaces.

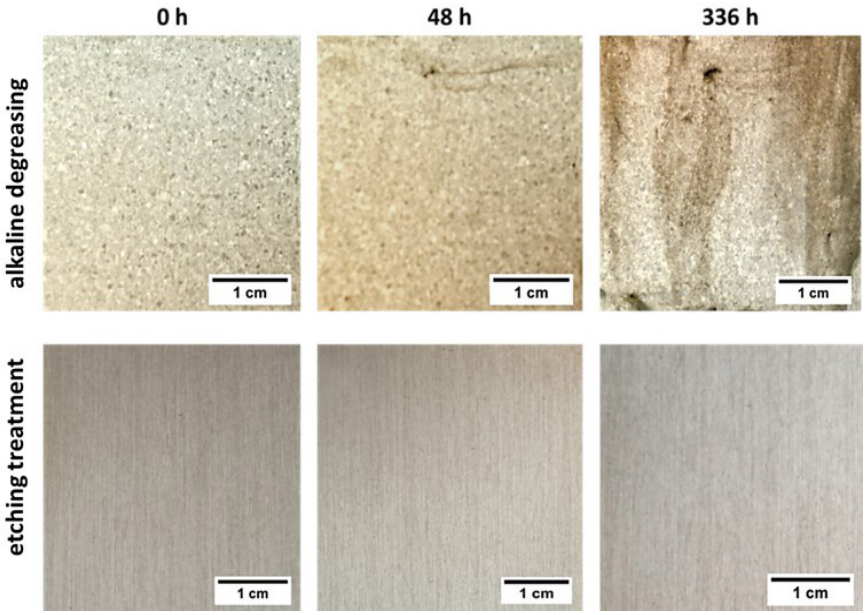


**Figure 9.** Macrographs of AA2198-T851 samples after alkaline degreasing (top) or etching (bottom) followed by TSA-anodizing and exposure to the NSST test (ASTM B-117).

## 4. Discussion

The results demonstrate that etching pretreatment removed coarse intermetallic (IM) particles, and this greatly affected the morphology, composition, and corrosion performance of the anodic aluminum oxide (AAO) coating on AA2198-T851. SEM images reveal a higher pore density on the etched sample compared to the alkaline degreased one, suggesting that the properties of the oxide film is greatly affected by the coarse IM particles on the surface.

According to the field-assisted dissolution theory proposed by O'Sullivan and Wood[52], the porous layer develops after the barrier layer formation, driven by continuous ionic flow and electrolyte access to the metal/oxide interface, leading to localized oxide dissolution[44,52]. The equilibrium between the oxide formation rate (at the metal/oxide interface) and the oxide dissolution rate (at the oxide/electrolyte interface) determines the final pore structure. Pore nucleation is associated with localized electric field concentrations caused by defects or non-uniform oxide thickness[40,44,52].

The current density-time response during anodizing further supports this effect. The etched sample exhibits a more gradual current increase during the pore nucleation stage compared to the alkaline-degreased sample, indicating that removal of coarse IM particles contributes to a more uniform electric field distribution during anodic film growth. EDS analysis of the etched surface did not reveal copper-enriched areas associated with IM particles, suggesting that the absence of Cu-rich sites promotes a more homogeneous pore distribution during nucleation, as observed in the FEG-SEM images.

The modifications in the barrier layer due to intermetallic (IM) particle removal were also reflected in the EIS results, which showed that the etched sample presented a more compact barrier with fewer conductive pathways for electrolyte penetration. These findings are consistent with the NSST results, in which only the etched sample showed no visible corrosion after 336 hours of exposure.

It is important to clarify that the detrimental incorporation of copper into the anodic oxide layer, as discussed in the literature, is primarily observed when coarse Cu-rich intermetallics are present on the surface before anodizing[39,53-55]. Under these conditions, $Cu^{+}$ or $Cu^{2+}$ ions can migrate into the forming oxide, reduce its resistivity, and promote oxygen evolution, leading to void formation and localized film degradation[39,40,42,53,54]. This behavior was previously reported in our recent work[55], where we demonstrated that the low solubility of copper oxides in acidic anodizing electrolytes causes trapping and accumulation of Cu species, which in turn facilitates electrolyte access to the underlying matrix and increases susceptibility to localized corrosion.

The improved corrosion resistance observed in the etched condition is attributed to the prior removal of these copper-containing intermetallics, which prevents such side reactions from occurring during anodizing. This interpretation is supported by the theoretical framework developed by Runge[56,57], who emphasized that anodic oxide formation is governed by interfacial chemical potential gradients rather than by field-assisted ionic migration alone. According to her analysis, the presence of intermetallic particles at the metal/oxide interface disrupts local equilibrium conditions, leading to uneven film growth and the development of microstructural discontinuities.

Additionally, Runge highlighted that the initial surface condition, particularly the distribution and chemical nature of intermetallic particles, plays a decisive role in determining the uniformity and protective quality of the anodic film. In this context, a cleaner aluminum surface, free from copper-rich phases, favors a more uniform electric field distribution, reduces defect formation, and enables the development of a compact and protective anodic oxide layer.

The differences in AAO layer composition were also observed in XPS results. The Al 2p high-resolution spectra of the etched sample exhibited a single component ($Al_2O_3$ film), whereas the alkaline-degreased sample displayed three components (Al°, $Al_2O_3$, and AlOOH). This difference suggests that the etched sample has a more homogeneous surface composition and a less defective oxide layer, as the absence of Al° and AlOOH components indicates fewer voids and impurities within the film.

Overall, these findings confirm that etching pretreatment enhances the corrosion resistance of TSA-anodized AA2198-T851 by removing coarse IM particles, promoting a more uniform electric field distribution, reducing Cu-rich defect sites, and improving barrier layer integrity.

## 5. Conclusions

a. The surface treatment that led to the removal of coarse IM particles through etching prior to anodizing resulted in a more homogeneous anodic film both, in morphology and composition, compared to alkaline degreasing, which led to partial removal of these particles.

b. The alkaline-degreasing treatment retained coarse IM particles on the surface, and this resulted in defective sites in the anodic film. These defects acted as preferential sites for corrosion nucleation, making the surface more susceptible to localized attack. In contrast, the etched surface led to a less defective oxide layer formed by anodizing, reducing the likelihood of localized corrosion initiation.

c. The pore distribution in the anodic film formed on the etched surface was more homogeneous than on the alkaline-degreased sample. This improvement was attributed to the removal of coarse IM particles, leading to a better electric field distribution during anodizing, and consequently promoting more uniform pore formation.

d. The etching pretreatment not only resulted in a more homogeneous pore distribution but also produced a higher pore density.

## 6. Acknowledgements

The authors gratefully acknowledge the financial support provided by São Paulo Research Foundation (FAPESP) under grant numbers 2019/18388-1 and 2022/06935-0.

## 7. References

1. Harvey TG. Cerium-based conversion coatings on aluminium alloys: a process review. Corros Eng Sci Technol. 2013;48(4):248-69. http://doi.org/10.1179/1743278213Y.0000000089.
2. Kulinich SA, Akhtar AS. On conversion coating treatments to replace chromating for Al alloys: recent developments and possible future directions. Russ J Non-Ferrous Met. 2012;53(2):176-203. http://doi.org/10.3103/S1067821212020071.
3. Pantelakis SG, Chamos AN, Kermanidis AT. A critical consideration for the use of Al-cladding for protecting aircraft aluminum alloy 2024 against corrosion. Theor Appl Fract Mech. 2012;57(1):36-42. http://doi.org/10.1016/j.tafmec.2011.12.006.
4. Demopoulos J. Corrosion resistance of silane coatings on aluminum and magnesium alloys. Honors Res Proj. 2017;551:1-25.
5. Alam MP, Sinha AN. Fabrication of third generation Al–Li alloy by friction stir welding: a review. Sadhana. 2019;44(6):1-13. http://doi.org/10.1007/s12046-019-1139-4.
6. Frankel GS. Pitting corrosion of metals. J Electrochem Soc. 1998;145(6):2186-98. http://doi.org/10.1149/1.1838615.
7. Moreto JA, Gamboni OC, Marino CEB, Bose Filho W, Fernandes JCS, Rocha LA. Corrosion behavior of Al and Al-Li alloys used as aircraft materials. Corros Prot Mater. 2012;31(3–4):60-4.
8. Alexopoulos ND. Artificial ageing of aeronautical Al–Cu–Li (2198) sheets: mechanical behaviour and corrosion susceptibility. Eng Proc. 2025;90:82. http://doi.org/10.3390/engproc2025090082.
9. Moreto JA, Broday EE, Rossino LS, Fernandes JCS, Bose Filho WW. Effect of localized corrosion on fatigue–crack growth in 2524-T3 and 2198-T851 aluminum alloys used as aircraft materials. J Mater Eng Perform. 2018;27(4):1917-26. http://doi.org/10.1007/s11665-018-3244-7.
10. Moreto JA, Gambonf O, Rucherf COFT, Romagnoli F, Moreira MF, Beneduce F, et al. Corrosion and fatigue behavior of new Al alloys. Procedia Eng. 2011;10:1521-6. http://doi.org/10.1016/j.proeng.2011.04.254.
11. Wanhill RJH, Bray GH. Aerostructural design and its application to aluminum-lithium alloys. In: Prasad NE, Gokhale A, Wanhill RJH, editors. Aluminum-lithium alloys: processing, properties, and applications. Oxford: Elsevier; 2014. p. 27–58. http://doi.org/10.1016/B978-0-12-401698-9.00002-1.
12. Donatus U, Terada M, Ospina CR, Queiroz FM, Bugarin AFS, Costa I, et al. On the AA2198-T851 alloy microstructure and its correlation with localized corrosion behaviour. Corros Sci. 2018;131:300-9. http://doi.org/10.1016/j.corsci.2017.12.001.
13. Ma YE, Xia ZC, Jiang RR, Li WY. Effect of welding parameters on mechanical and fatigue properties of friction stir welded 2198 T8 aluminum–lithium alloy joints. Eng Fract Mech. 2013;114:1-11. http://doi.org/10.1016/j.engfracmech.2013.10.010.
14. Donatus U, Klumpp RE, Mogili NVV, Antunes RA, Milagre MX, Costa I. The effect of surface pretreatment on the corrosion behaviour of silanated AA2198-T851 Al–Cu–Li alloy. Surf Interface Anal. 2019;51(2):275-89. http://doi.org/10.1002/sia.6584.
15. Araujo JVDS, Queiroz FM, Terada M, Astarita A, Costa I. EIS study of the microstructure influence on the corrosion behaviour of AA2198-T3 compared to AA2198-T851 alloy. In: XXX International Conference on Surface Modification Technologies; 2016 June 29-July 1; Milan. Proceedings. Milan: Politecnico di Milano; 2016.
16. Gao C, Zhu Z, Han J, Li H. Correlation of microstructure and mechanical properties in friction stir welded 2198-T8 Al–Li alloy. Mater Sci Eng A. 2015;639:489-99. http://doi.org/10.1016/j.msea.2015.05.038.
17. Donatus U, Araujo JVDS, Machado C SC, Mogili NVV, Antunes RA, Costa I. The effect of manufacturing process induced near-surface deformed layer on the corrosion behaviour of AA2198-T851 Al–Cu–Li alloy. Corros Eng Sci Technol. 2018;2782:1-11.
18. Machado CSC, Donatus U, Milagre MX, Mogili NV, Giorjão RAR, Klumpp RE. Araujo JVDS, Ferreira RO, Costa I. Correlating the modes of corrosion with microstructure in friction stir welded AA2198-T8 alloy in aqueous hydrogen peroxide-chloride medium. Corrosion. 2019;75(6):628-40. http://doi.org/10.5006/3054.
19. Klumpp RE, Donatus U, Araujo JVS, Redígolo MM, Machado CSC, Costa I. The effect of acid pickling on the corrosion behavior of a cerium conversion-coated AA2198-T851 Al–Cu–Li alloy. J Mater Eng Perform. 2020;29(1):167-74. http://doi.org/10.1007/s11665-019-04551-9.
20. Hughes AE, Harvey TG, Nikpour T, Muster TH, Hardin SG. Non-chromate deoxidation of AA2024-T3 using Fe(III)–HF–$HNO_3$. Surf Interface Anal. 2004;36:15-23.

21. Araujo JVS, Silva RMP, Klumpp RE, Costa I. O processo de anodização do alumínio e suas ligas: uma abordagem histórica e eletroquímica. Quim Nova. 2021;44(8):999-1011. http://doi.org/10.21577/0100-4042.20170748.
22. Capelossi VR, Poelman M, Recloux I, Hernandez RPB, de Melo HG, Olivier MG. Corrosion protection of clad 2024 aluminum alloy anodized in tartaric-sulfuric acid bath and protected with hybrid sol-gel coating. Electrochim Acta. 2014;124:69-70. http://doi.org/10.1016/j.electacta.2013.09.004.
23. Lee W, Park SJ. Porous anodic aluminum oxide: anodization and templated synthesis of functional nanostructures. Chem Rev. 2014;114(15):7487-556. http://doi.org/10.1021/cr500002z.
24. Rioja RJ, Liu J. The evolution of Al-Li base products for aerospace and space applications. Metall Mater Trans, A Phys Metall Mater Sci. 2012;43(9):3325-37. http://doi.org/10.1007/s11661-012-1155-z.
25. Dursun T, Soutis C. Recent developments in advanced aircraft aluminium alloys. Mater Des. 2014;56:862-71. http://doi.org/10.1016/j.matdes.2013.12.002.
26. Araujo JVS, Milagre M, Costa I. Milagre M, Costa I. A historical, statistical and electrochemical approach on the effect of microstructure in the anodizing of Al alloys: a review. Crit Rev Solid State Mater Sci. 2023;49(4):521-81. http://doi.org/10.1080/10408436.2023.2230250.
27. Araujo J, Pereira R, Klumpp R, Costa I. O processo de anodização do alumínio e suas ligas: uma abordagem histórica e eletroquímica. Quim Nova. 2021;44(8):999-1011. http://doi.org/10.21577/0100-4042.20170748.
28. Ma Y, Zhou X, Liao Y, Chen X, Zhang C, Wu H, et al. Effect of anodizing parameters on film morphology and corrosion resistance of AA2099 aluminum-lithium alloy. J Electrochem Soc. 2016;163(7):369-76. http://doi.org/10.1149/2.1081607jes.
29. Wu H, Ma Y, Huang W, Zhou X, Li K, Liao Y, et al. Effect of iron-containing intermetallic particles on film structure and corrosion resistance of anodized AA2099 alloy. J Electrochem Soc. 2018;165(9):573-81. http://doi.org/10.1149/2.1361809jes.
30. Machado CSC, Klumpp RE, Ayusso VH, Donatus U, Milagre MX, Araujo JV S, et al. Effect of surface treatments on the localized corrosion resistance of the AA2198-T8 aluminum lithium alloy welded by FSW process. Surf Interface Anal. 2019;51(12):1231-39.
31. Ma Y, Zhou X, Liao Y, Yi Y, Wu H, Wang Z, et al. Localised corrosion in AA 2099-T83 aluminium-lithium alloy: the role of grain orientation. Corros Sci. 2016;107:41-8. http://doi.org/10.1016/j.corsci.2016.02.018.
32. Klumpp RE, da Silva RMP, Donatus U, Machado C S, Ayusso VH, Milagre MX, et al. Influência da composição da solução de tratamento de superfície na resistência à corrosão da liga AA2024-T3. Tratamento de Superfície. 2019;212:23-8.
33. Monetta T, Acquesta A, Maresca V, Signore R, Bellucci F, Di Petta P, et al. Characterization of aluminum alloys environmentally friendly surface treatments for aircraft and aerospace industry. Surf Interface Anal. 2013;45(10):1522–1529.
34. Klumpp RE, Donatus U, Maria R, Antunes RA, Milagre MX, Costa I, et al. Corrosion protection of the AA2198-T8 alloy by environmentally friendly organic-inorganic sol-gel coating based on bis-1,2-(triethoxysilyl)ethane. Surf Interface Anal. 2020;53(3):314-29. http://doi.org/10.1002/sia.6919.
35. Araujo JVS, Chen J, Zhou X, Costa I. Investigation of corrosion behaviour in anodized new generation aluminium alloys. In: EFC's Annual Conference; 2023 Aug 27-31; Brussels. Proceedings. Brussels: European Federation of Corrosion; 2023. v. 63.
36. Araujo JVS, Milagre MX, Zhou X, Costa I. An assessment of pitting corrosion in anodized aluminum alloys: it might not be what it seems. Mater Corros. 2024;75(5):599-613. http://doi.org/10.1002/maco.202313977.
37. Araujo JV, Milagre MX, Gabbardo AD, Klumpp RE, Costa I. The effect of tartaric-sulfuric acid (TSA) anodizing on the corrosion resistance of the AA7475-T761. ECS Meet Abstr. 2022;MA2022-02(14):2475.
38. Araujo JVS, Milagre MX, Klumpp RE, Ayusso VH, Donatus U. Costa I. TSA anodising voltage effects on the near-surface coarse intermetallic particles in the AA2024-T3 and AA2198-T8 alloys. Corros Eng Sci Technol. 2022;57(4):380-96. http://doi.org/10.1080/1478422X.2022.2071666.
39. Curioni M, Saenz de Miera M, Skeldon P, Thompson GE, Ferguson J. Macroscopic and local filming behavior of AA2024 T3 aluminum alloy during anodizing in sulfuric acid electrolyte. J Electrochem Soc. 2008;155(8):C387. http://doi.org/10.1149/1.2931522.
40. Ma Y, Zhou X, Thompson GE, Curioni M, Hashimoto T, Skeldon P, et al. Anodic film formation on AA 2099-T8 aluminum alloy in tartaric–sulfuric acid. J Electrochem Soc. 2011;158(2):C17. http://doi.org/10.1149/1.3523262.
41. Ma Y, Zhou X, Liao Y, Chen X, Zhang C, Wu H, et al. Effect of anodizing parameters on film morphology and corrosion resistance of AA2099 aluminum-lithium alloy. J Electrochem Soc. 2016;163(7):C369-76. http://doi.org/10.1149/2.1081607jes.
42. Curioni M, Skeldon P, Koroleva E, Thompson GE, Ferguson J. Role of tartaric acid on the anodizing and corrosion behavior of AA2024-T3 aluminum alloy. J Electrochem Soc. 2009;156(4):C147. http://doi.org/10.1149/1.3077602.
43. Curioni M, Skeldon P, Thompson GE. Anodizing of aluminum under nonsteady conditions. J Electrochem Soc. 2009;156(12):C407-13. http://doi.org/10.1149/1.3230642.
44. Martínez-Viademonte MP, Abrahami ST, Hack T, Burchardt M, Terryn H. A review on anodizing of aerospace aluminum alloys for corrosion protection. Coatings. 2020;10(11):1-30. http://doi.org/10.3390/coatings10111106.
45. Hitzig J, Jüttner K, Lorenz WJ. AC-impedance measurements on corroded porous aluminum oxide films. J Electrochem Soc. 1986;133(5):5-10. http://doi.org/10.1149/1.2108756.
46. Hinder SJ, Grilli R, Rustame M, Santos WIA, Baker MA, Costa I. A surface analytical investigation of cerium-based conversion coatings deposited onto an AA2024-T3 aluminium alloy cladding layer. Surf Interface Anal. 2014;46(Feb):735-9. http://doi.org/10.1002/sia.5440.
47. Hughes AE, Taylor RJ, Hinton BRW, Wilson L. XPS and SEM characterization of hydrated cerium oxide conversion coatings. Surf Interface Anal. 1995;23(7–8):540-50. http://doi.org/10.1002/sia.740230714.
48. Cornette P, Zanna S, Seyeux A, Costa D, Marcus P. The native oxide film on a model aluminium-copper alloy studied by XPS and ToF-SIMS. Corros Sci. 2020;174:108837. http://doi.org/10.1016/j.corsci.2020.108837.
49. Fayed SM, Gao P, Chen D, Li S, Zhou Y, Wang H, et al. Corrosion inhibition characteristics of multilayer Si-DLC, phosphating and anodizing coatings deposited on 2024 Al alloy: a comparative study. Diamond Related Materials. 2021;117:108460. http://doi.org/10.1016/j.diamond.2021.108460.
50. Ura-Binczyk E, Homazava N, Ulrich A, Hauert R, Lewandowska M, Kurzydlowski KJ, et al. Passivation of Al-Cr-Fe and Al-Cu-Fe-Cr complex metallic alloys in 1 M $H_2SO_4$ and 1 M NaOH solutions. Corros Sci. 2011;53(5):1825-37. http://doi.org/10.1016/j.corsci.2011.01.061.
51. Dhanish S, Yoganandan G, Balaraju JN. Development of TSA anodized/MnVO sealed coating using a statistical approach for Al 7075 alloy and a study of its corrosion behaviour. Surf Coat Tech. 2020;402:126316. http://doi.org/10.1016/j.surfcoat.2020.126316.
52. O'Sullivan JP, Wood GC. The morphology and mechanism of formation of porous anodic films on aluminium. Proc R Soc Lond A Math Phys Sci. 1970;317(1531):511-43. http://doi.org/10.1098/rspa.1970.0129.
53. Iglesias-Rubianes L, Garcia-Vergara J, Skeldon P, Thompson GE, Ferguson J, Beneke M. Challenges of the metallic fuselage. Electrochim Acta. 2007;54(24):7148-57.
54. Elabar D, La Monica GR, Santamaria M, Di Quarto F, Skeldon P, Thompson GE. Anodizing of aluminium and AA 2024-T3 alloy in chromic acid: effects of sulphate on film growth. Surf Coat Tech. 2017;309:480-9. http://doi.org/10.1016/j.surfcoat.2016.11.108.

55. Araujo JVS, Chen J, Costa I, Zhou X. Localized corrosion in anodized aluminium alloys: the role of constituent particle-induced defects in anodic films. Corros Sci. 2025;252:1-24. http://doi.org/10.1016/j.corsci.2025.112961.
56. Runge JM, Hossain T. Interfacial phenomena in 7000 series alloys and their impact on the anodic oxide. Mater Today Proc. 2015;2(10):5055-62. http://doi.org/10.1016/j.matpr.2015.10.096.
57. Runge JM, Pomis AJ. Impact of surface treatment and interfacial phenomena on the anodizing process. Annual Technical Conference & Exhibit—AESF SUR/FIN® '99/American Regional INTERFINISH; 1999 June 21-24; Cincinnati. Proceedings. Cincinatti: AESF; 1999. p. 21–24.

## Data Availability

The entire dataset supporting the results of this study was published in the article itself.